

© 2016, Elsevier. Licensed under the Creative Commons Attribution-NonCommercial-NoDerivatives 4.0 International
<http://creativecommons.org/licenses/by-nc-nd/4.0/>

Evaluation of undrained failure envelopes of caisson foundations under combined loading

Moura Mehravar (corresponding author), PhD, MSc, BSc

Wolfson School of Mechanical and Manufacturing Engineering
Loughborough University
Leicestershire, United Kingdom
LE11 3TU
E-mail: M.Mehravar@lboro.ac.uk

Ouahid Harireche, PhD, MSc, BSc

Islamic University in Madinah, KSA
Faculty of engineering
Department of civil engineering
E-mail: O.Harireche@gmail.ac.uk

Asaad Faramarzi, PhD, MSc, BSc

School of Civil Engineering,
The University of Birmingham
Edgbaston, Birmingham B15 2TT, United Kingdom
Tel: +44 (0) 121 414 5050
E-mail: A.Faramarzi@bham.ac.uk

1 Evaluation of undrained failure envelopes of 2 caisson foundations under combined loading

Abstract

3 In this paper, results of a three-dimensional finite element study addressing the effect of
4 embedment ratio (L/D) of caisson foundations on the undrained bearing capacity under
5 uniaxial and combined loadings are discussed. The undrained response of caisson
6 foundations under uniaxial vertical (V), horizontal (H) and moment (M) loading are
7 investigated. A series of equations are proposed to predict the ultimate vertical, moment
8 and maximum horizontal bearing capacity factors. The undrained response of caisson
9 foundations under combined $V-H$ and $V-M$ load space is studied and presented using
10 failure envelopes generated with side-swipe method. The kinematic mechanism
11 accompanying failure under uniaxial loading is addressed and presented for different
12 embedment ratios. Predictions of the uniaxial bearing capacities are compared with other
13 models and it is confirmed that the proposed equations appropriately describe the
14 capacity of caisson foundations under uniaxial vertical, horizontal and moment loading in
15 homogenous undrained soils. The results of this paper can be used as a basis for standard
16 design codes of off-shore skirted shallow foundations which will be the first of its kind.

17 **Keywords:** bearing capacity; caisson; shallow foundation; three-dimensional finite
18 element modelling; undrained analysis.

1 Introduction

19 A suction caisson consists of a thin-walled upturned ‘bucket’ of cylindrical shape made
20 from steel. This type of foundation has proven to be efficient and versatile as a support
21 for offshore structures and appears to be a very attractive option for future use in offshore
22 wind turbines [1-4]. The thin caisson wall facilitates installation when a pressure
23 differential is induced by suction on the caisson lid, which pushes the caisson to penetrate
24 into the seabed. This is achieved by pumping out the water trapped in the caisson cavity
25 after initial penetration under self-weight [5-8]. The skirt can improve the foundation
26 bearing capacity by trapping the soil between them during undrained loading [9-10]. A
27 number of studies have been conducted on the investigation of bearing capacities of
28 caisson foundations. However, in the most of the former studies the foundation was either
29 analysed as a skirted strip foundation using finite element analyses (FEA) and upper
30 bound solutions or as a surface circular foundation using three-dimensional FEA without
31 considering the skirt length in the simulation [11-20]. On the other hand, offshore
32 foundations are three-dimensional and embedded. The skirt length has a considerable
33 impact on their bearing capacities. Only few studies were performed by considering the
34 caisson foundation using three-dimensional model. Most of these analyses did not
35 comprehensively cover a wide range of practical embedment ratios or investigate all
36 vertical, horizontal and moment bearing capacities [21-22]. A summary of previous
37 studies on undrained bearing capacities and failure envelopes of shallow foundations are
38 presented in Table 1.

39

Table 1

40 In the present study the main objective is to perform three-dimensional (3D) undrained
41 numerical simulations to predict the bearing capacity of caisson foundations under
42 uniaxial and combined loading conditions. The present study refers mainly to the work
43 done by Gourvernec [18], Bransby and Randolph [11], which are essentially plane strain
44 analyses. It has been justified that within such context, the assumption of full bonding
45 between the caisson and surrounding soil is plausible (especially that suction
46 development at the interface in undrained condition prevents separation). Hence, the
47 work performed in the current paper has been limited to a similar context, taking
48 advantage of efficient numerical computations and reasonable computational time. An
49 extension of the present work by implementing interfaces would shed more light on the
50 accuracy of both plane strain and 3D models, but such an extension is beyond the scope
51 of the present paper.

52 In this paper, a series of three-dimensional finite element analyses using ABAQUS [23]
53 are performed to investigate the effect of the embedment depth on the bearing capacity of
54 shallow foundations in homogenous undrained soil. Different aspect ratios of caisson
55 foundation “ $L/D = 0, 0.25, 0.5, 0.75, 1$ ”, where L is the embedment length and D is the
56 caisson diameter are considered. Uniaxial vertical (V), horizontal (H) and moment (M)
57 bearing capacities are investigated and presented as a series of equations to estimate the
58 uniaxial ultimate vertical, moment and maximum horizontal bearing capacity factors of
59 caisson foundations. Finally, the capacities of caisson foundations under combined VH ,
60 VM load space are studied and expressed by failure envelopes.

61

62

63 **2 Numerical modelling**

64 **2.1 Model geometry and mesh**

65 In order to obtain precise results, a series of three-dimensional finite element analyses
66 were carried out for the practical range of embedment ratios, $L/D = 0$ (surface
67 foundation), 0.25, 0.5, 0.75 and 1 in a homogenous undrained soil profile. It is important
68 to cover a wide range of values starting from the special case of a surface foundation and
69 moving towards moderately deep foundations ($L/D \leq 1$). However, the number of aspect
70 ratio investigated has been kept to a reasonable maximum to keep the simulation concise
71 and comprehensive.

72 Taking advantage of the symmetrical nature of the problem, only half of the entire system
73 was modelled. Figure 1 shows a semi-cylindrical section through a diametrical plane of a
74 caisson foundation with $L/D=0.5$. This figure also represents the typical finite element
75 mesh for caisson foundation, used in this study. A number of different mesh densities in
76 which element sizes around the caisson wall and tip are considerably refined were
77 performed to obtain accurate results in a reasonable computational time. The mesh is
78 extended $5D$ from the caisson foundation centre line and top of the soil, respectively so
79 that the failure loads are not sensitive by their position or to the boundary conditions. The
80 caisson thickness is considered $4 \times 10^{-3} D$, which reflects a reasonable value for typical
81 caisson foundations. Displacements in all three coordinate directions (x , y and z) at the
82 bottom of the base of the mesh were completely fixed, and also normal displacements on
83 the lateral boundaries were prevented.

Figure 1

84 The caisson foundation nomenclature and the sign convention which is adopted in this
85 study are presented in Figure 2.

Figure 2

86 In order to model the soil, first-order, eight-node linear brick, reduced integration
87 continuum with hybrid formulation element (C3D8RH) is employed. The hybrid
88 elements are appropriate to model the behaviour of near-incompressible materials such as
89 undrained soils [18].

90 **2.2 Material modelling**

91 In this study the soil is modelled as a linear elastic-perfectly plastic material based on the
92 Tresca failure criterion ($\phi = 0^\circ$) with an effective unit weight $\gamma' = 6\text{kN/m}^3$ and Poisson's
93 ratio $\nu = 0.49$. The undrained shear strength of the clay are considered as $S_u = 5\text{kPa}$ with an
94 undrained young's modulus to undrained shear strength ratio (E_u / S_u) of 500. The
95 foundations are modelled physically as rigid bodies with a Young's modulus of $E = 10^9$
96 E_u and $\gamma = 78\text{ kN/m}^3$. The interface between soil and foundation was fully bonded so that
97 there is no detachment between the soil and the foundation [13]. This assumption for
98 interface is particularly relevant to caisson foundations since they have a significant uplift
99 capacity, especially for short term loading [11] and the developed suction at the interface
100 prevents separation in undrained condition. A tensile resistance develops at the foundation
101 level under undrained loading condition due to suction pressure within the soil plug.

102 **2.3 Loading path**

103 In this study the loading is applied using a displacement-controlled method by prescribing
104 vertical (w), horizontal translation (u) or rotation (θ) at the reference point RP (Figure 2).
105 It should be mentioned that, due to the capability to predict post-failure conditions, the
106 displacement-controlled method, is more appropriate than the stress-controlled method
107 for achieving failure loads [14, 24-25]. In order to obtain failure envelopes in V - H and V -
108 M spaces the so-called “side-swipe” test is performed. This method was firstly used by
109 Tan [26] during his centrifuge test, and consists of two stages. Initially, a given
110 displacement at one direction (typically vertical) is applied to the foundation until
111 bringing the foundation to the failure condition. In the second stage, displacement in
112 other degrees of freedom is prescribed whilst the vertical displacement increment is set to
113 zero and the foundation is “swiped” either horizontally or in rotation. The stress path in
114 the second stage can almost define the shape of the failure envelope because the elastic
115 stiffness is much larger than the plastic stiffness. Advantageously, this method is able to
116 determine a large section of the failure envelope in a single test.

117 **3 Finite element analysis results**

118 **3.1 Vertical bearing capacity**

119 Firstly, it should be mentioned that to achieve results which can be applied to any caisson
120 geometry and undrained soil strength the obtained data from this study are normalised
121 with respect to the foundation diameter (D) and undrained soil strength (S_u). Figure 3 and
122 Figure 4 show the predicted variation of normalised vertical load versus normalised
123 vertical displacement (w/D) and the vertical bearing capacity factor ($N_{cv} = F_v/A.S_u$), in

124 which A is area of the caisson horizontal cross section) as a function of various
125 embedment ratios (L/D), respectively.

Figure 3

Figure 4

126 Figure 4 shows that the vertical bearing capacity increased non-linearly by increasing the
127 embedment ratio. This confirms the effect of the skirt length in enhancing the vertical
128 bearing capacity of caisson foundations. However, a smaller rate of the increasing trend is
129 observed for $L/D \geq 0.7$. This phenomenon can be explained as being due to the changing
130 failure mechanism for an increasing skirt length from the traditional Prandtl theory of
131 surface foundations (Figure 5a), and such a mechanism switch to a confined failure
132 mechanism for a long skirt (Figure 5b).

Figure 5 (a-b)

133 Based on the three-dimensional finite element results obtained from this study, a
134 quadratic relationship is proposed to predict the vertical capacity depth factor

135 $d_{cv} = N_{cv(\frac{L}{D})} / N_{cv(\frac{L}{D}=0)}$ of caisson foundations (Figure 6), in which $N_{cv(\frac{L}{D}=0)} = 6.2$. It
 136 should be mentioned that this proposed equation is valid only for an embedment ratio
 137 range, $0 \leq L/D \leq 1$. For embedment ratios beyond this range the equation should be
 138 applied with care and further simulations are required.

139

$$d_{cv} = -0.28\left(\frac{L}{D}\right)^2 + \left(\frac{L}{D}\right) + 1 \quad (1)$$

Figure 6

140 **3.1.1 Comparing vertical bearing capacity with other published data**

141 The results for vertical bearing capacity factors are compared with other published data.
 142 For the circular surface foundation ($L/D=0$), a vertical bearing capacity factor $N_{cv} = 6.2$
 143 was obtained which represents an overestimation of 2.5% compared to the exact solutions
 144 of $V_{ult} = 6.05 A.S_u$ [27-29]. Table 2 presents a brief comparison between the vertical
 145 bearing capacity factors of circular surface foundation proposed by different approaches.

Table 2

146 It should be highlighted that exact solutions of the vertical bearing capacity of skirted
 147 strip or embedded three-dimensional foundations are not available. However, for
 148 comparison, an upper bound solution for a fully rough, embedded strip foundation has

149 been obtained by Bransby and Randolph [11], and Plane-strain finite element results for
150 fully rough caisson foundations have been conducted by Gourvenec [18]. A prediction
151 from the conventional vertical depth factor [30] is also presented in Figure 7.

Figure 7

152 It can be seen from Figure 7 that the values of the undrained vertical bearing capacity of
153 caisson foundation based on Skempton's depth factor are considerably small compared to
154 the prediction by either this study or other published data for a rough foundation. For
155 instance, the conventional Skempton's method underestimated the amount of vertical
156 bearing capacity by more than a 45% for $L/D = 0.5$. Indeed, although conventional depth
157 factors have been applied to rough and smooth, circular and strip foundations, they have
158 been originally suggested for smooth-sided circular foundations [18]. In other words, the
159 bearing capacity predicted by the conventional method does not consider the contribution
160 of the friction between skirt and soil.

161 Additionally, a comparison between this study and a finite element analysis performed by
162 Gourvenec [18] indicates that, using a plane-strain analysis for caisson foundation
163 underestimates the vertical bearing capacity factor (e.g about 17% for $L/D = 1$). This
164 difference can be explained by the fact that in a 2D analysis, the effects of foundation
165 shape and soil-structure interaction are not considered properly. Meanwhile, a three-
166 dimensional analysis allows the additional soil deformation mechanism to be taken into
167 consideration.

168 The upper bound solution by Bransby and Randolph [11] also underestimates the actual
169 bearing capacity. Because the caisson foundation was described using a two-dimensional
170 model. It should be also noted that since in the upper bound solution, the effect of an
171 increasing embedment ratio (L/D) on the failure mechanism has not been considered, the
172 linear increasing trend of vertical bearing capacity is not beyond the expectation.

173 **3.2 Maximum horizontal bearing capacity**

174 Figure 8 and Figure 9 present the normalised results of the variation of maximum
175 horizontal load ($F_{h \text{ (max)}}$) against horizontal displacement ratio (u/D) and the maximum
176 horizontal bearing capacity factor ($N_{ch \text{ (max)}} = F_{h \text{ (max)}} / A.S_u$) as a function of various
177 embedment ratios (L/D), respectively. In this section the maximum horizontal loads and
178 bearing capacity correspond to pure horizontal translation ($u > 0$ and θ is constrained).

Figure 8

Figure 9

179 In contrast with the nonlinear smooth increasing trend for $L/D \geq 0.7$ which was observed
 180 for the ultimate vertical bearing capacity factor of caisson foundations, Figure 9 revealed
 181 that maximum horizontal bearing capacity increasing rate with an increasing embedment
 182 ratio (L/D) is linear. The main reason is, when rotation is constrained and pure horizontal
 183 translation is applied, no coupling between rotation and horizontal degree of freedom
 184 develops. Hence, a pure sliding mechanism occurs for all embedment ratios.
 185 Figure 10 (a-d) show the failure mechanism under pure horizontal translation using
 186 incremental displacement vectors for different embedment ratios.

Figure 10(a-d)

187 Based on these results a linear relationship can be expressed to explain the maximum
 188 horizontal depth factor $d_{ch(\max)} = N_{ch(\max)(\frac{L}{D})} / N_{ch(\max)(\frac{L}{D}=0)}$ for the embedment ratios up to
 189 unity, where $N_{ch(\max)(\frac{L}{D}=0)} = 1$.

$$d_{ch(\max)} = 7.5 \left(\frac{L}{D} \right) + 1 \quad (2)$$

Figure 11

190 **3.2.1 Comparing horizontal bearing capacity with other published data**

191 The calculated results for maximum horizontal bearing capacity factor by Gourvenec [18]
192 and Bransby and Randolph [11] are shown in Figure 12, and are compared to the obtained
193 result in this study.

Figure 12

194 Figure 12 indicates that all above predictions for $N_{ch(max)}$ show a linear increasing trend
195 for embedment ratios up to unity. However, both predictions by Gourvenec [18] and
196 Bransby and Randolph [11] of the maximum horizontal bearing capacity of caisson
197 foundation based on Plane-strain and upper bound solution respectively, underestimated
198 the bearing capacity. The main reason is that in both cases, the problem was considered as
199 two dimensional. Hence, the effect of foundation shape was not reflected in their
200 predictions.

201 Furthermore, in order to demonstrate the effect of kinematic failure mechanism on the
202 horizontal capacity of embedded foundations, the ultimate horizontal bearing capacity
203 obtained through a three-dimensional finite element analysis under pure horizontal load
204 by Hung and Kim [21] is presented and compared with the calculated maximum
205 horizontal bearing capacity obtained in this study by applying pure sliding (Figure 13). It
206 should be noted that the ultimate bearing capacity (subscripted by 'ult') corresponds to
207 the pure horizontal load ($\theta \neq 0$).

Figure 13

208 It can be observed from Figure 13 that there is a non-linear increasing rate of ultimate
209 horizontal bearing capacity which is smaller for $0.25 \leq L/D \leq 0.5$, while the maximum
210 horizontal bearing capacity increases linearly. The main reason can be explained by the
211 difference between the failure mechanisms in maximum and ultimate horizontal bearing
212 capacities. Indeed, when pure horizontal translation is applied to the foundation level,
213 there is no coupling between horizontal and rotation degrees of freedom and the pure
214 sliding mechanism governs failure, while under pure horizontal loading condition, there
215 exists a coupling between horizontal and rotation degrees of freedom, which can cause
216 both horizontal and rotation displacements. Additionally, under pure horizontal loading
217 when $0.25 \leq L/D \leq 0.5$ no coupling between horizontal and rotation degree of freedom
218 was observed by [21], therefore the difference between the ultimate and maximum
219 horizontal bearing capacity is small (Figure 13).

220 In addition, it can be clearly observed that, for $L/D \geq 0.75$ the difference between ultimate
221 and maximum horizontal bearing capacities becomes more significant. This indicates that
222 under pure horizontal loading the effect of coupling becomes more considerable with an
223 increasing embedment ratio (L/D), since the failure mechanism activates more rotation
224 and less sliding. Consequently, the three-dimensional finite element analysis confirms
225 that by constraining the rotation degree of freedom ($\theta = 0$) of a caisson foundation,
226 horizontal bearing capacity can be enhanced (e.g. about 46% for $L/D=1$).

227 **3.3 Ultimate moment bearing capacity**

228 Figure 14 and Figure 15 present the normalised results of the variation of ultimate
229 moment load (M_{ult}) against normalised rotational degree of freedom (θ/D) and the
230 ultimate moment capacity as a function of various embedment ratios (L/D), respectively.
231 It should be mentioned that in this section ultimate moment load and capacity correspond
232 to the pure moment load ($\theta > 0$ and u is not constrained), which means that when a pure
233 moment is applied at foundation level, both rotation and horizontal degrees of freedom
234 affect the failure mechanism.

Figure 14

Figure 15

235 These figures reveal that by increasing the embedment ratio, the ultimate bearing capacity
236 of the caisson foundations increases non-linearly. However, for embedment ratios (L/D) \geq
237 0.75, the increasing rate of ultimate moment capacity decreases. This can be justified by
238 the fact that at larger embedment depth, the effect of coupling between horizontal and
239 rotational degrees of freedom becomes more discernible. Indeed, at larger embedment
240 depths, more sliding and less rotation accompany the failure mechanism. Figure 16 (a-d)
241 shows the failure mechanism under pure moment load by incremental displacement
242 vectors for various embedment ratios.

Figure 16(a-d)

243 The scoop mechanism can be detected from Figure 16(a-d) for the failure mechanism
244 under pure moment load, in which there exists a clear distance between the rotation
245 centre and the foundation tip. In addition, by increasing the embedment length, the centre
246 of rotation tends to move towards the foundation level.

247 Based on these obtained results the following quadratic equation is proposed to express
248 the ultimate moment capacity depth factor $d_{ch(ult)} = N_{ch(ult)(\frac{L}{D})} / N_{ch(ult)(\frac{L}{D}=0)}$, in which

249 $N_{ch(ult)(\frac{L}{D}=0)} = 0.55$.

$$d_{cm(ult)} = -0.37\left(\frac{L}{D}\right)^2 + 2.54\left(\frac{L}{D}\right) + 1 \quad (3)$$

Figure 17

250 **3.3.1 Comparison of the ultimate moment bearing capacity with other published data**

251 The calculated results for the ultimate moment bearing capacity factor by Gourvenec [18]
252 and Bransby and Randolph [11] are presented in Figure 18. These results are compared to
253 the three-dimensional finite element predictions performed in this study.

Figure 18

254 It can be observed from Figure 18 that for embedment ratios less than 0.5 there is no
255 significant difference between the predicted results by this study and those achieved with
256 a plane-strain finite element analysis [18]. A similar observation can be made regarding
257 the comparison with the upper bound by Bransby and Randolph [11]. This later solution
258 is based on a cylindrical scoop cutting the edge of the foundation.

259 However, the difference becomes more pronounced as the embedment ratio increases
260 (e.g. $L/D > 0.7$). This discrepancy reflects the fact that a three-dimensional analysis takes
261 into account the foundation shape, which is ignored in the two-dimensional model. In
262 fact, the effect of foundation shape clearly indicates that by increasing the embedment
263 ratios (e.g. $L/D \geq 0.7$) the increasing rate of ultimate moment capacity decreases due to
264 the effect of coupling between rotation and horizontal degrees of freedom. Hence, for
265 larger embedment ratios, more sliding and less rotation govern the failure mechanism
266 Figure 16(a-d).

267 **3.4 Failure envelopes**

268 Failure envelopes provide a practical way to visualise the behaviour of foundations under
269 combined loading conditions. For loading conditions inside the envelope, the foundation
270 response is elastic. The boundary of the envelope corresponds to the yielding of the
271 foundation. Mainly, side-swipe test and constant displacement method which are both
272 based on displacement control have been used by various researchers to capture the shape
273 of the yield-locus. In this study, side-swipe method is employed to obtain failure
274 envelopes under combined vertical-horizontal and vertical- moment loading conditions.

275 As it was mentioned in section 2.3 this method was used for the first time by Tan [26].
276 The first and second stages of the side-swipe method are shown in Figure 19 by probes
277 AB and BC respectively. Probe AB is obtained by prescribing a given displacement
278 (typically vertical) to the foundation until the ultimate load is reached. At the next stage,
279 indicated by the probe BC in Figure 19 a second displacement (horizontal or rotational) is
280 prescribed to the foundation while the vertical displacement increment is set to zero.

Figure 19

3.4.1 *Combined horizontal and vertical loading (zero moment load)*

281 Figure 20 show the obtained failure envelopes under combined vertical and horizontal
282 loading conditions for different embedment ratios ($L/D=0, 0.25, 0.5, 0.75, 1$),
283 respectively. It is clear that there is no difference between the shapes of the failure
284 envelopes for all embedment depths. However, by increasing embedment ratios the
285 failure envelopes expand, which confirms the effect of the embedment depth on
286 increasing the load carrying capacity. On the other hand, this expanding rate decreases for
287 embedment ratios beyond 0.75 roughly. It can be also seen that in the presence of
288 horizontal loading, the vertical bearing capacity factor (N_{cv}) decreases.

Figure 20

289 **3.4.2 Combined vertical and moment loading (zero horizontal load)**

290 Figure 21 illustrate the failure envelopes under combined vertical-moment loading of
291 caisson foundations for different embedment ratios $L/D = 0, 0.25, 0.5, 0.75$ and 1. These
292 figures indicate that, despite their similar shape, the failure envelopes have a size that
293 expands for an increasing embedment ratio (L/D). However, for $L/D \geq 0.75$ this
294 expanding rate decreases. This phenomenon confirms the efficiency of using caisson
295 foundations compared with shallow surface foundation to enhance vertical-moment
296 bearing capacity. Figure 21 also reveals that decreasing in moment loading accompanying
297 utilisation the ultimate vertical capacity.

Figure 21

298 **4 Conclusion**

299 In this paper a series of three-dimensional finite element analyses have been conducted
300 with ABAQUS in order to evaluate the uniaxial undrained bearing capacity factors as
301 well as to obtain failure envelopes in the $V-H$ and $V-M$ spaces for caisson foundations at
302 various embedment ratios ($(L/D)= 0, 0.25, 0.5, 0.75, 1$). Based on the simulation results
303 three individual equations have been proposed for the ultimate vertical and moment as
304 well as maximum horizontal depth factor. Additionally, the results of uniaxial bearing
305 capacity factors were compared with proposed solutions and obtained results by other
306 studies.

307 An increasing trend was observed in the value of the ultimate vertical bearing capacity
308 factor for an increasing embedment ratio. However, the results (Fig 4 and Fig 6) indicate
309 that such an increase is less pronounced for $L/D \geq 0.7$, due to the transition of the failure
310 mechanism as it was illustrated in Fig 5(a-b).

311 On the other hand, the maximum horizontal bearing capacity is found to increase linearly
312 for embedment ratios up to unity. The numerical simulations revealed that under pure
313 horizontal translation, a pure sliding mechanism governs failure. Moreover, the maximum
314 horizontal bearing capacities were compared with the ultimate horizontal capacity of
315 caisson foundations and have indicated that constraining the rotation degree of freedom
316 causes an improvement in the horizontal bearing capacity of caisson foundations.

317 The results have shown that the rate of ultimate moment capacity decreases for
318 embedment ratios $(L/D) \geq 0.75$, which can be explained to be due to the fact that at larger
319 embedment depths, more sliding and less rotation accompanies the failure mechanism.

320 Moreover, the failure mechanism under maximum horizontal load and ultimate moment
321 and vertical loading were investigated for different embedment ratios (L/D) . Under
322 ultimate moment loads (when the horizontal displacement is not constrained), scoop
323 mechanism was observed with a centre point that lies above the caisson tip, but moves
324 towards it for an increasing embedment ratio. The results achieved in this paper can be
325 used as a basis for standard design codes of off-shore skirted shallow foundations which
326 will be the first of its kind. For all mentioned embedment ratios, side-swipe tests were
327 conducted to obtain yield loci as well as failure envelopes in $V-H$ and $V-M$ spaces and
328 similar shapes were observed. The results indicated that the failure envelopes expand for
329 an increasing embedment ratio, in which the expansion rate for approximately $L/D \geq 0.75$
330 decreased.

331

332

References:

- [1] Tjelta, T. I. & Haaland, G., 1993. Novel foundation concept for a jacket finding its place. *Offshore site investigation and foundation behaviour*, Volume 28, pp. 717-728.
- [2] Byrne, B. W., Houlsby, G. T., Martin, C. & Fish, P., 2002. Suction caisson foundations for offshore wind turbines. *Wind Enineering*, 26(3), pp. 145-155.
- [3] Byrne, B. W. & Houlsby, G. T., 2003. Foundation for offshore wind turbines. *Philosophical Transactions of the Royal Society of London*, 361(Series A), pp. 2909-2930.
- [4] Luke, A. M., Rauch, A. F., Olson, R. E. & Mecham, E. C., 2005. Component of suction caisson capacity measured in axial pullout tests. *Ocean Engineering*, Volume 32, pp. 878-891.
- [5] Houlsby, G. T. & Byrne, B. W., 2005. Design procedures for installation of suction caissons in sand. *Proceedings of the Institution of Civil Engineers, Geotechnical Engineering*, 158(GE3), pp. 135-144.
- [6] Harireche, O., Mehravar, M. & Alani, A. M., 2013. Suction caisson in stallation in sand with isotropic permeability varying with depth. *Applied Ocean Research*, Volume 43, pp. 256-263.
- [7] Harireche, O., Mehravar, M. & Alani, A. M., 2014. Soil conditions and bounds to suction during the installation of caisson foundations in sand. *Ocean Engineering*, Volume 88, pp. 164-173.
- [8] Mehravar, M., Harireche, O., Faramarzi, A., Alani, A.M. 2015. Modelling the Variation of suction pressure during caisson installation in sand using FLAC3D. *Ships and Offshore Structures*, pp. 1-7.
- [9] Tani, K. & Craig, W. H., 1995. Bearing capacity of circular foundations on soft clay of strength increasing with depth. *Soils Found*, 35(4), pp. 21-35.
- [10] Bransby, M. F. & Randolph, M. F., 1998. Combined loading of skirted foundations. *Geotechnique*, 48(5), pp. 637-655.
- [11] Bransby, M. F. & Randolph, M. F., 1999. The effect of embedment depth on the undrained response of skirted foundations to combined loading. *Soil and Foundations*, 39(4), pp. 19-33.
- [12] Gourvenec, S. & Barnett, S., 2011. Undrained failure envelope for skirted foundations under general loading. *Geotechnique*, 61(3), pp. 263-270.
- [13] Bransby, M. F. & Yun, G. J., 2009. The undrained capacity of skirted strip foundations under combined loading. *Geotechnique*, 59(2), pp. 115-125.

- [14] Gourvenec, S. & Randolph, M., 2003. Effect of non-homogeneity on the shape of failure envelopes for combined loading of strip and circular foundations on clay. *Geotechnique*, 53(6), pp. 575-586.
- [15] Randolph, M. F., & Puzrin, A. M., 2003. Upper bound limit analysis of circular foundations on clay under general loading. *Geotechnique* **53**, No. 9, 785-796.
- [16] Gourvenec, S. (2007). Failure envelopes for offshore shallow foundations under general loading. *Geotechnique* **57**, No. 3, 715-728.
- [17] Yun, G & Bransby, M. F., 2007. The undrained vertical bearing capacity of skirted foundations, *Soils and Found*, Vol 47, No 3, pp 493-505
- [18] Gourvenec, S., 2008. Effect of embedment on the undrained capacity of shallow foundations under general loading. *Geotechnique*, 58(3), pp. 177-185.
- [19] Taiebat, H. A. & Carter, J. P., 2010. A failure surface for shallow circular footing on cohesive soils. *Geotechnique* **60**, No. 4, 256-273.
- [20] Sukumaran, B., McCarron, W. O., JeanJean, P. & Abouseeda, H., 1999. Efficient finite element techniques for limit analysis of suction caissons under lateral loads. *Computers and Geotechnics*, Volume 24, pp. 89-107.
- [21] Hung, L. C. & Kim, S. R., 2012. Evaluation of vertical and horizontal bearing capacities of bucket foundations in clay. *Ocean Engineering*, Volume 52, pp. 75-82.
- [22] Vulpe, C., Gourvenec, S. & Power, M., 2014. A generalised failure envelope for undrained capacity of circular shallow foundations under general loading. *Geotechnique letter*, Volume 4, pp. 187-196.
- [23] Simulia, 2012. *ABAQUS user's manual*. Dassault Systemes Simulia Corp.
- [24] Houlsby, G. T. Martin, C. M., 2003. Undrained bearing capacity factors for conical footings on clay. *Geotechnique*, 53(5), pp. 513-520.
- [25] Bransby, M. F. & Randolph, M. F., 1997. Shallow foundations subject to combined loading. Wuhan, *Proceeding of the 9th international conference on computer methods in advanced in geomechanics*.
- [26] Tan, F. S., 1990. Centrifuge and theoretical modelling of conical footing on sand, Cambridge: PhD thesis, University of Cambridge.
- [27] Cox, A. D., Eason, G. & Hopkins, H. G., 1961. Axially symmetric plastic deformation in soils. *Philosophical Transaction of the Royal Society London*, 254(1036), pp. 1-45.
- [28] Houlsby, G. T. & Wroth, C. P., 1983. Calculation of stresses on shallow penetrometers and footings. Newcastle, *Proceedings of IUTAM/IUGG seabed Mechanics*.

[29] Martin, C. M., 2001. Vertical bearing capacity of skirted circular foundations on Tresca soil. Istanbul, *Proceeding of 15th International Conference on Soil Mechanics and Geotechnical Engineering*.

[30] Skempton, A. W., 1951. The bearing capacity of clays. London, *Proceedings of Building Research Congress*.

[31] Houlsby, G. T., Kelly, R. B., Huxtable, J. & Byrne, B. W., 2005. Field trials of suction caissons in clay for offshore wind turbine foundations. *Geotechnique*, 55(4), pp. 287-296.

List of Tables:

Table 1: A summary of studies on undrained bearing capacities of shallow foundation

Table 2: comparison with published data for N_{cv} of circle surface foundation

List of Figures:

Figure 1: Finite element mesh and boundary conditions

Figure 2: Foundation geometry

Figure 3: Normalised vertical load for different embedment ratios (L/D) vs normalised vertical displacement (w/D)

Figure 4: Vertical bearing capacity factor as a function of embedment ratio

Figure 5 (a-b): Failure mechanism under vertical load, (a) $L/D=0$ (surface foundation), (b) $L/D=1$

Figure 6: Vertical depth factor as a function of L/D ratios

Figure 7: Comparison of vertical bearing capacity

Figure 8: Normalised horizontal load for different embedment ratios (L/D) vs normalised horizontal displacement (u/D)

Figure 9: Maximum horizontal bearing capacity as a function of embedment ratio

Figure 10(a-d): Failure mechanism under horizontal load (h_{max} ; θ constrained), (a) $L/D=0.25$, (b) $L/D=0.5$, (c) $L/D=0.75$, (d) $L/D=1$

Figure 11: Maximum horizontal capacity depth factor as a function of L/D ratios

Figure 12: comparison of maximum horizontal bearing capacity predictions

Figure 13: A comparison between ultimate and maximum horizontal bearing capacity factors; $N_{ch(ult)}$ & $N_{ch(max)}$ when θ is constrained

Figure 14: Normalised moment for different embedment ratios (L/D) vs normalised rotation (θ/D)

Figure 15: Ultimate moment capacity as a function of embedment ratio

Figure 16 (a-d): Failure mechanism under moment load (M_{ult} ; u is not constrained), (a) $L/D=0.25$, (b) $L/D=0.5$, (c) $L/D=0.75$, (d) $L/D=1$

Figure 17: Ultimate moment capacity depth factor as a function of L/D ratios

Figure 18: Comparison of ultimate moment bearing capacity factor

Figure 19: A cross section of yield locus in V-H space using side-swipe method

Figure 20: Failure envelopes for vertical and horizontal loading space (moment load = 0)

Figure 21: Failure envelopes for vertical and moment loading space (horizontal load = 0)

Table 1: A summary of studies on undrained bearing capacities of shallow foundation

Footing Geometry	Embedment		Investigated capacity	Method	Reference
	Surface	Embedded			
Strip	√	–	<i>VHM</i>	FEM	Bransby & Randolph (1998)
Strip	–	√	<i>VHM</i>	FEM/UB	Bransby & Randolph (1999)
Strip, Circular	√	–	<i>VHM</i>	FEM	Gourvenec & Randolph (2003)
Circular	√	–	<i>VHM</i>	LUB	Randolph & Puzrin (2003)
Circular	√	–	<i>VHM</i>	FEM	Gourvenec (2007)
Strip	√	√	<i>V</i>	FEM/UB	Yun & Bransby (2007)
Strip	√	√	<i>VHM</i>	FEM	Gourvenec (2008)
Strip	–	√	<i>HM</i>	FEM/UB	Bransby & Yun (2009)
Circular	√	–	<i>VHM</i>	FEM	Taiebat & Carter (2010)
Circular	√	($L/D \leq 1$)	<i>VH</i>	FEM	Hung & Kim (2012)
Circular	√	($L/D \leq 0.5$)	<i>VHM</i>	FEM	Vulpe et al. (2014)
Circular	√	($0 \leq L/D \leq 1$)	<i>VHM</i>	FEM	This study

Table 2: Comparison with published data for N_{cv} of circle surface foundation

	Method	N_{cv}
This study	3D Finite element results	6.2
Gourvenec, 2008	2D Finite element results	5.21
Gourvenec and Randolph, 2003	3D Finite element results	5.91
Cox et al., 1961	Exact solution	6.05
Houlsby and Wroth, 1983		6.05
Martin, 2001		6.05

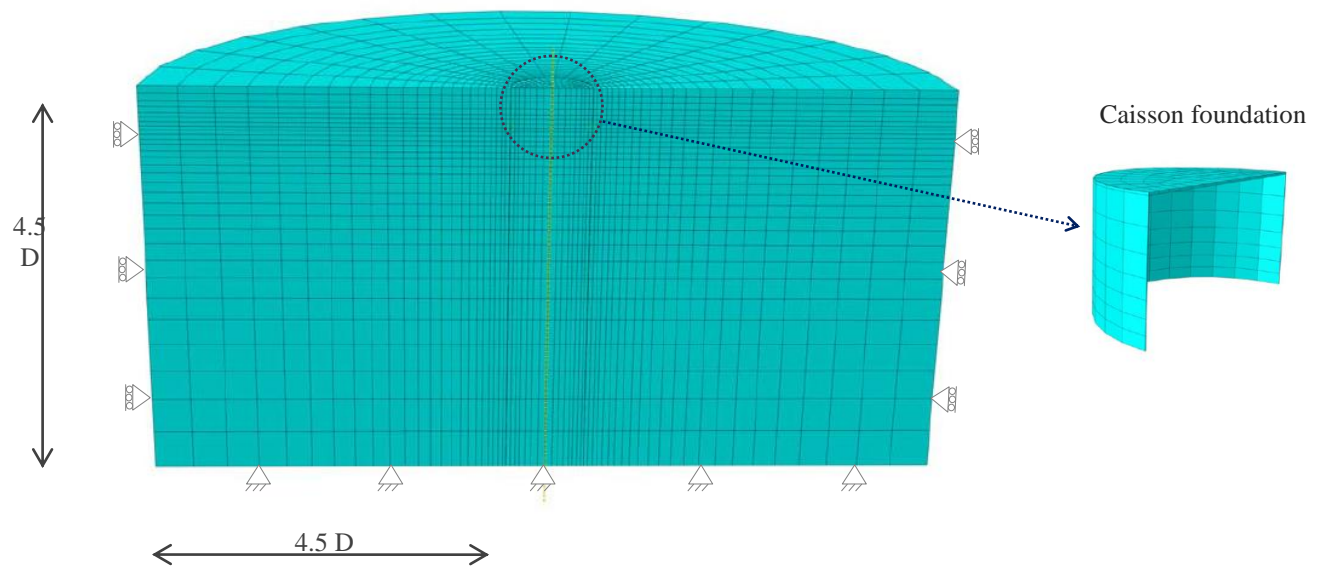


Figure 1: Finite element mesh and boundary conditions

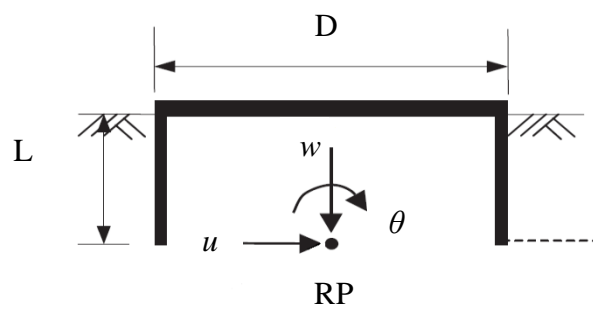


Figure 2: Foundation geometry

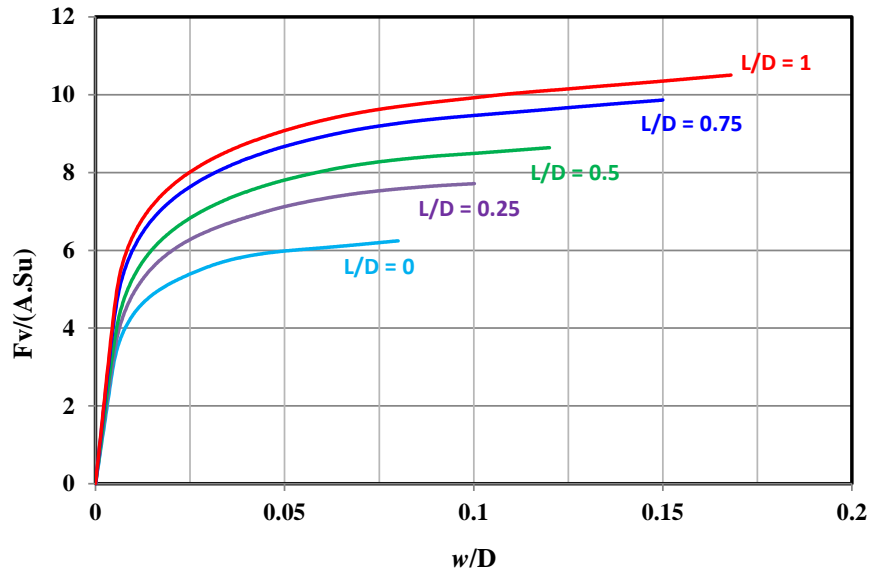


Figure 3: Normalised vertical load for different embedment ratios (L/D) vs normalised vertical displacement (w/D)

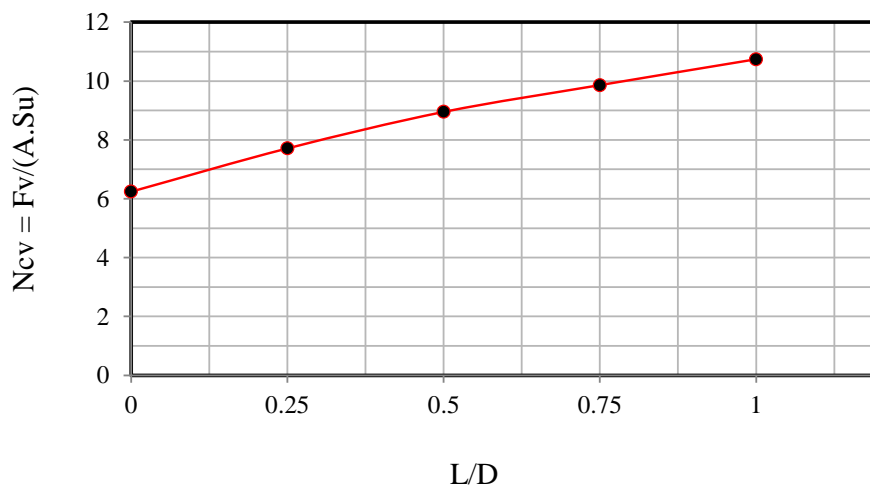
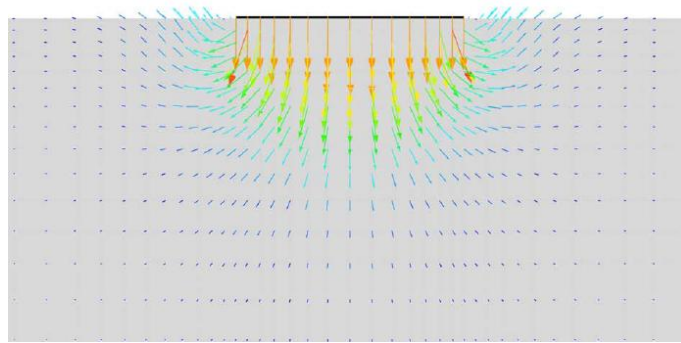
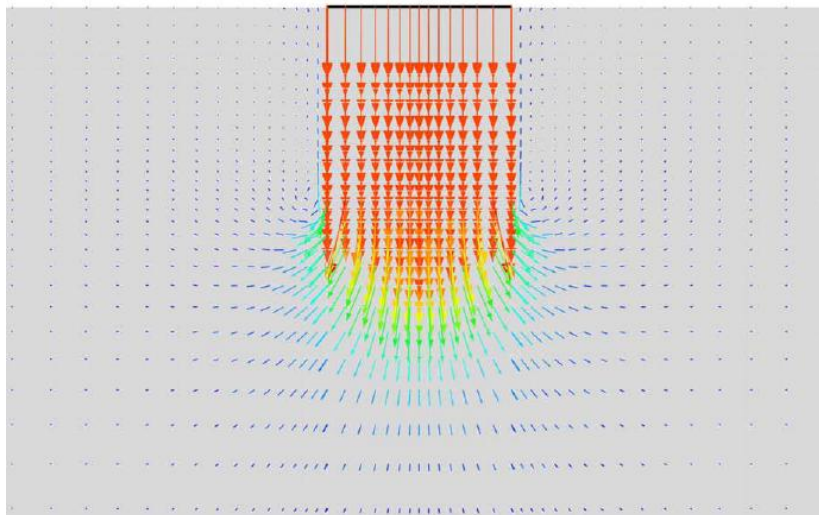


Figure 4: Vertical bearing capacity factor as a function of embedment ratio



(a)



(b)

Figure 5 (a-b): Failure mechanism under vertical load, (a) $L/D=0$ (surface foundation),
(b) $L/D=1$

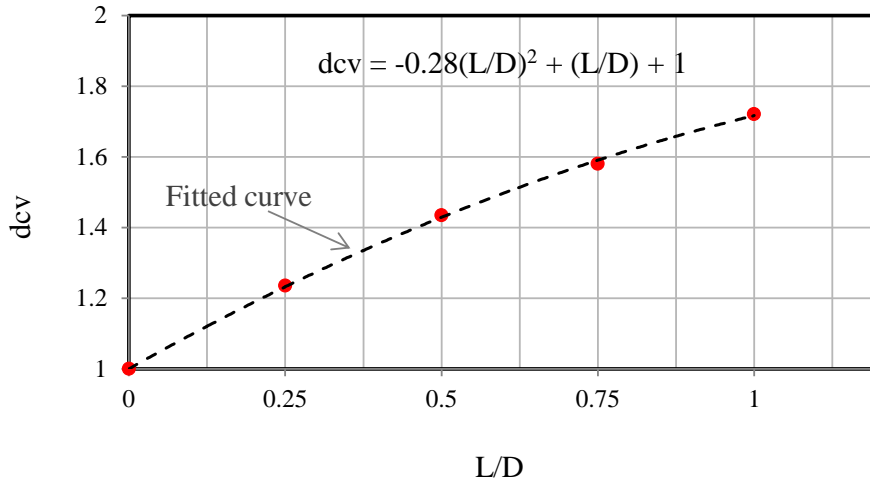


Figure 6: Vertical depth factor as a function of L/D ratios

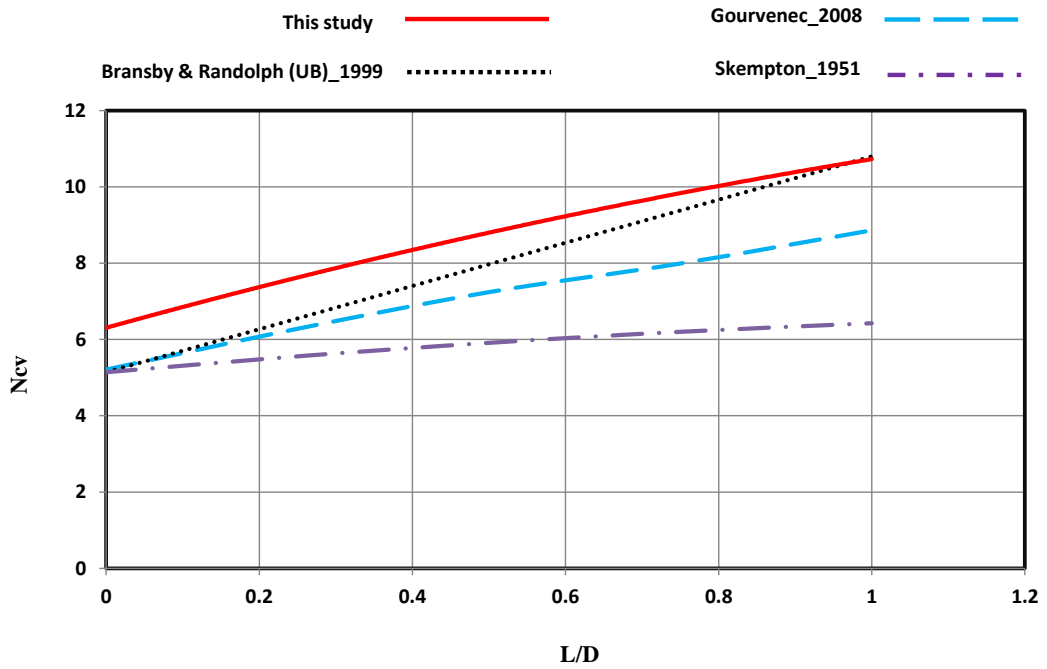


Figure 7: Comparison of vertical bearing capacity

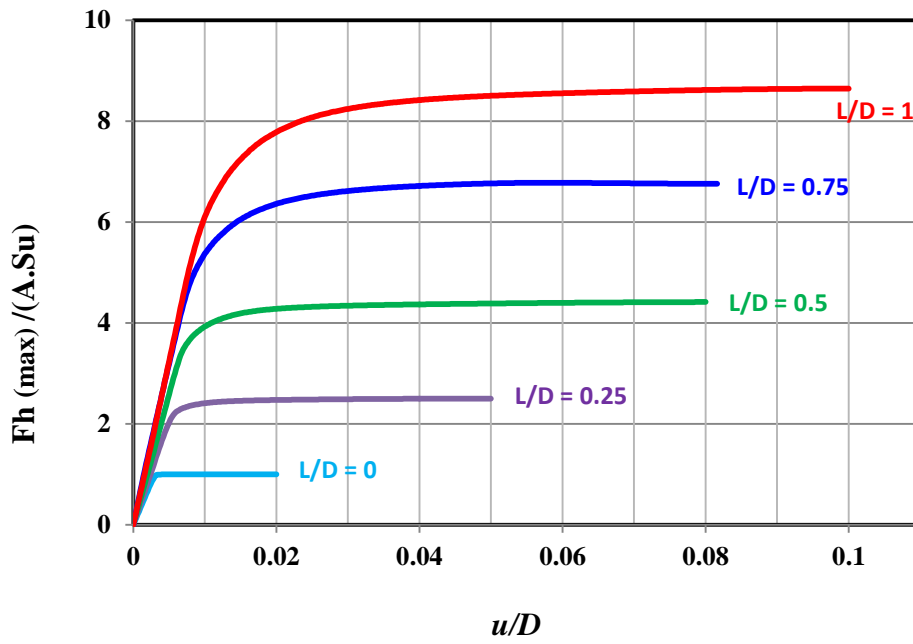


Figure 8: Normalised horizontal load for different embedment ratios (L/D) vs normalised horizontal displacement (u/D)

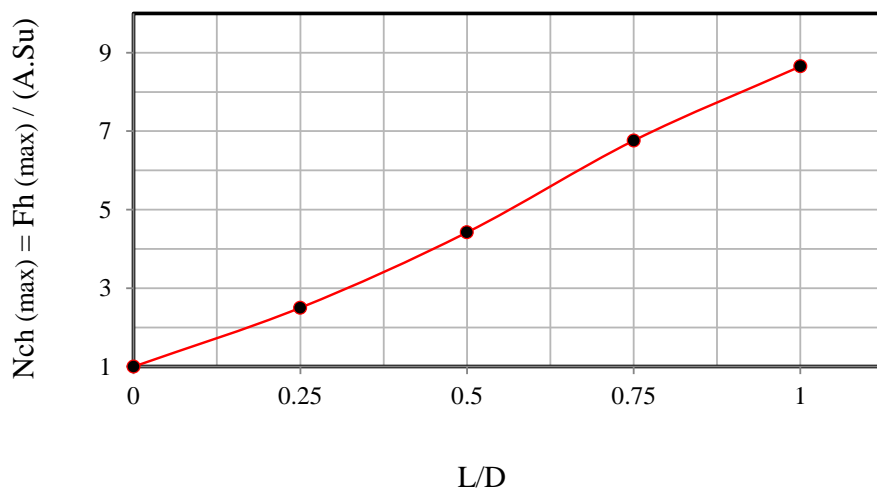
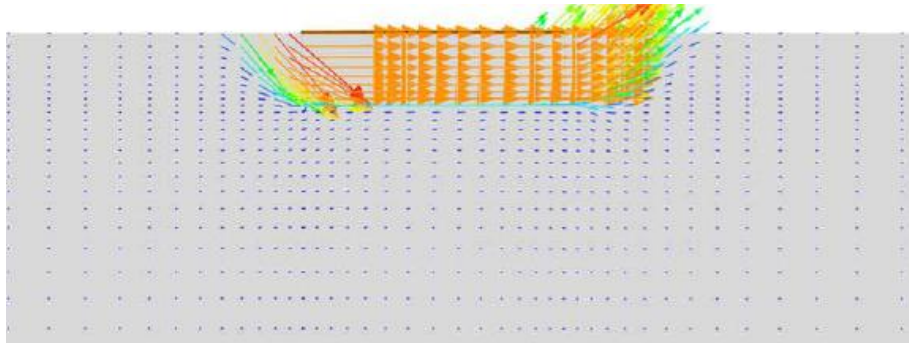
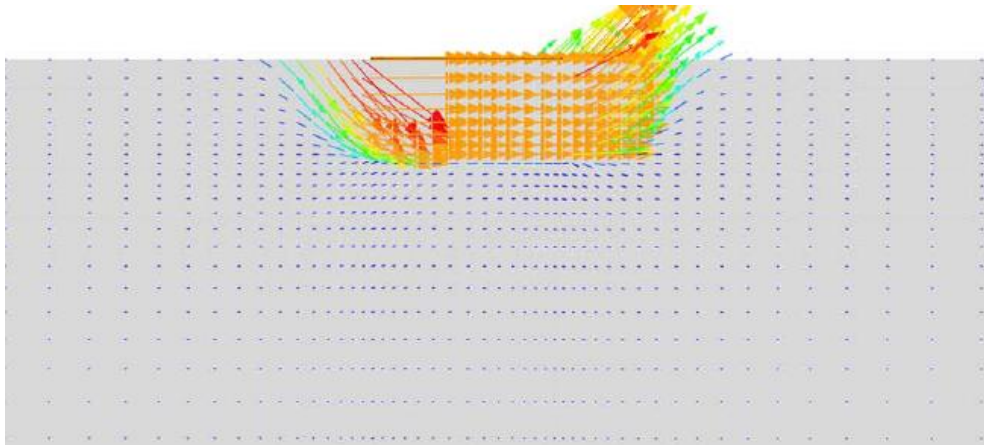


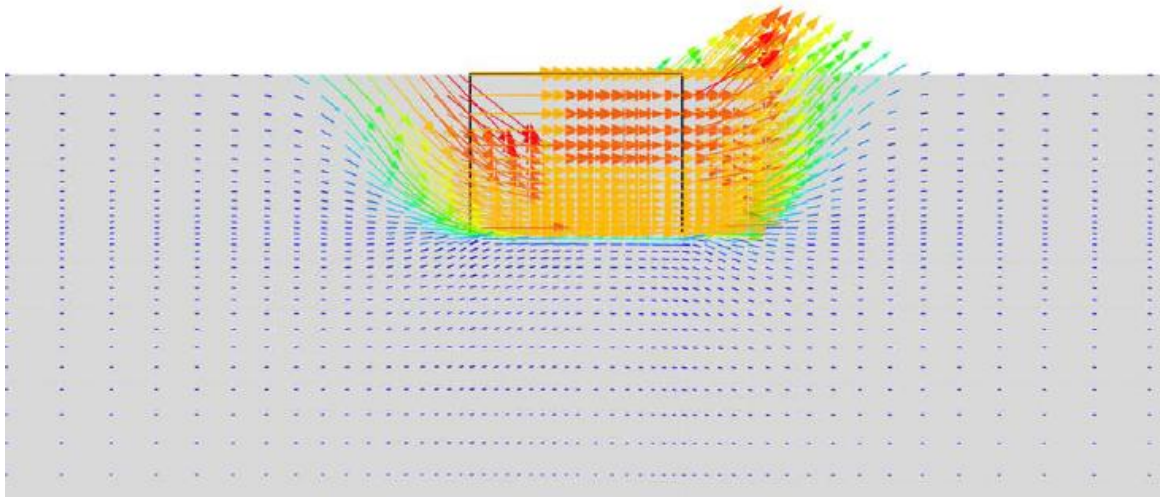
Figure 9: Maximum horizontal bearing capacity as a function of embedment ratio



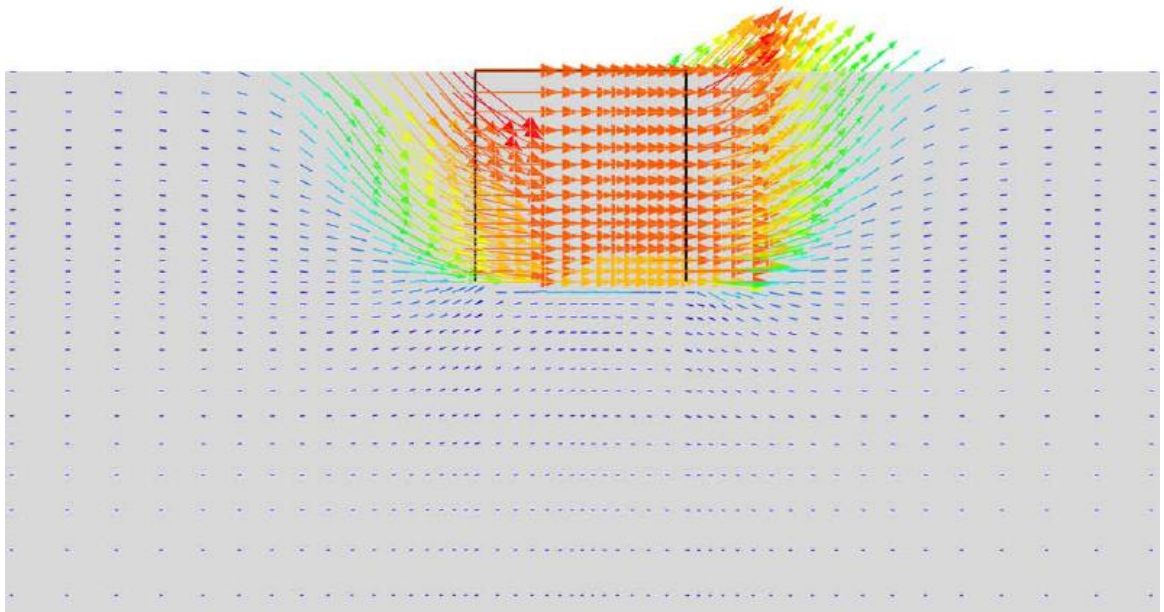
(a)



(b)



(c)



(d)

Figure 10(a-d): Failure mechanism under horizontal load (h_{max} ; θ constrained), (a) $L/D=0.25$, (b) $L/D=0.5$, (c) $L/D=0.75$, (d) $L/D=1$

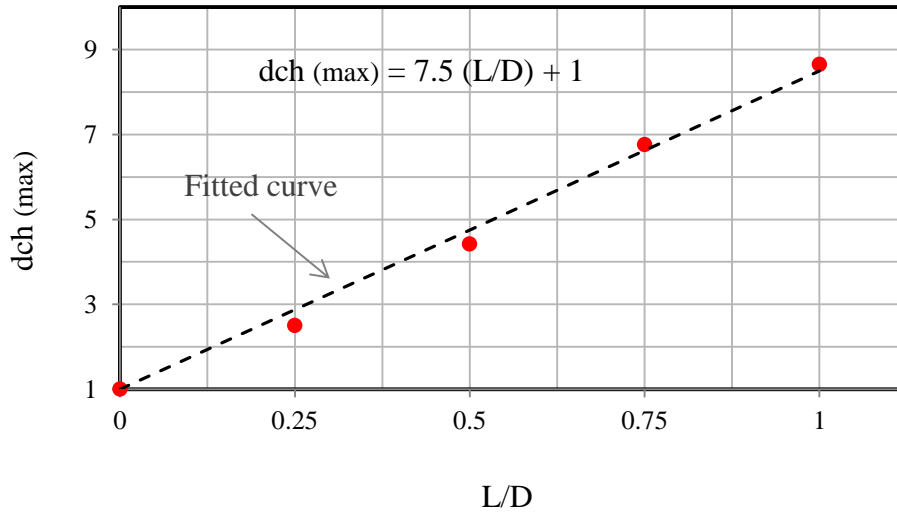


Figure 11: Maximum horizontal capacity depth factor as a function of L/D ratios

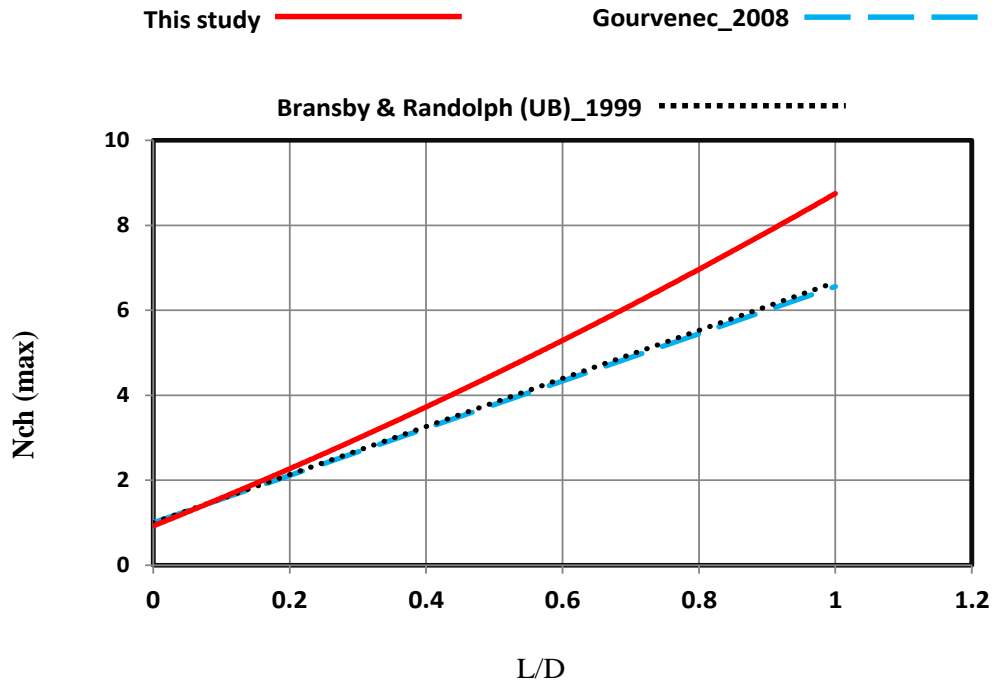


Figure 12: comparison of maximum horizontal bearing capacity predictions

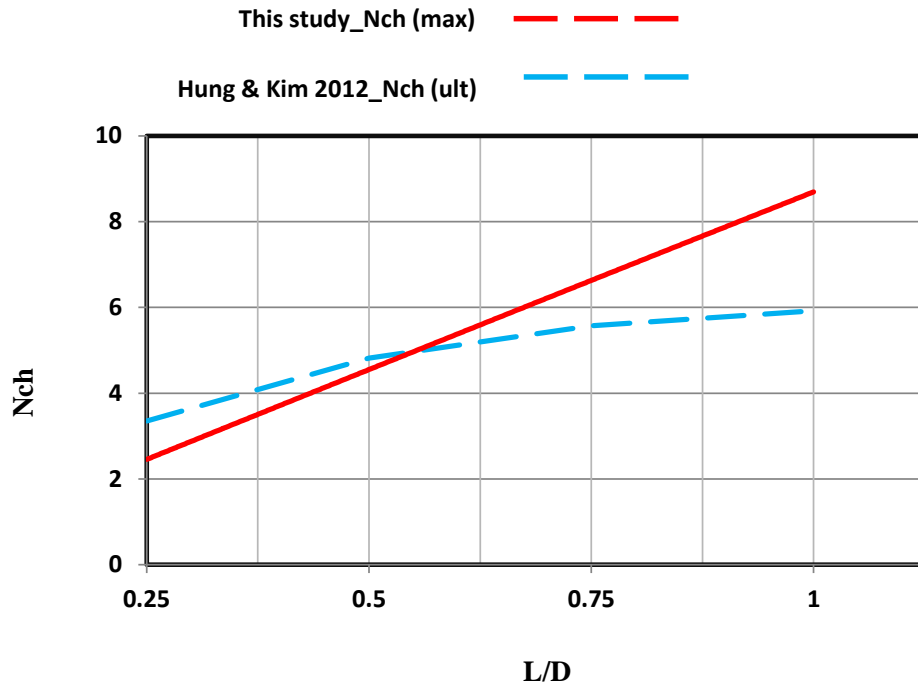


Figure 13: A comparison between ultimate and maximum horizontal bearing capacity factors; $N_{ch(ult)}$ & $N_{ch(max)}$ when θ is constrained

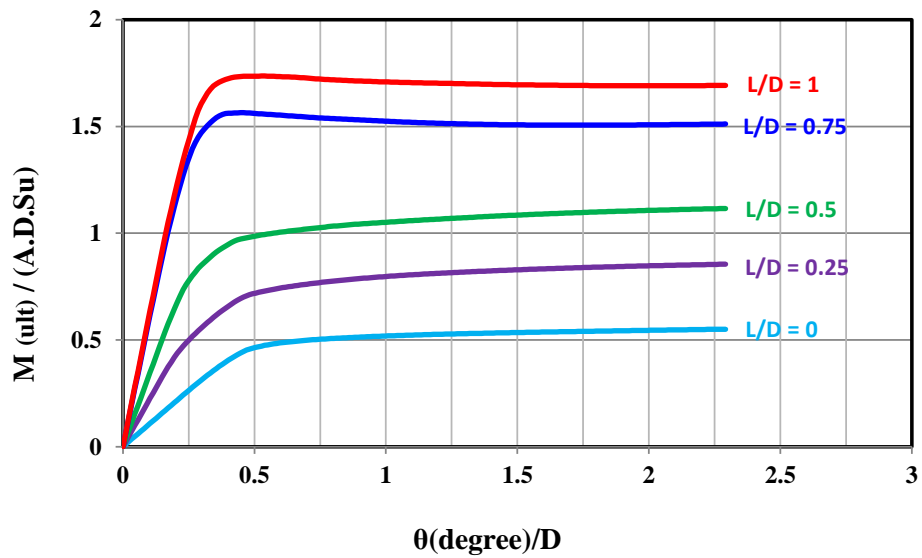


Figure 14: Normalised moment for different embedment ratios (L/D) vs normalised rotation (θ/D)

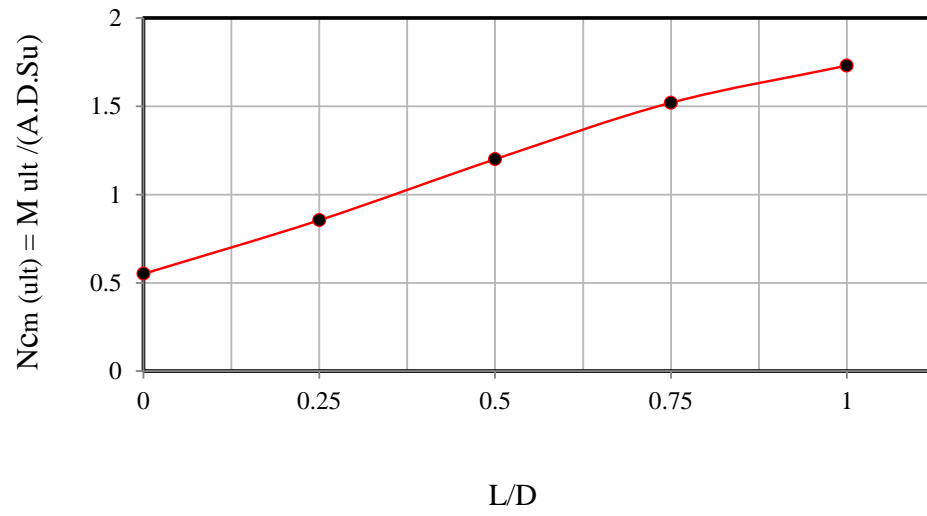
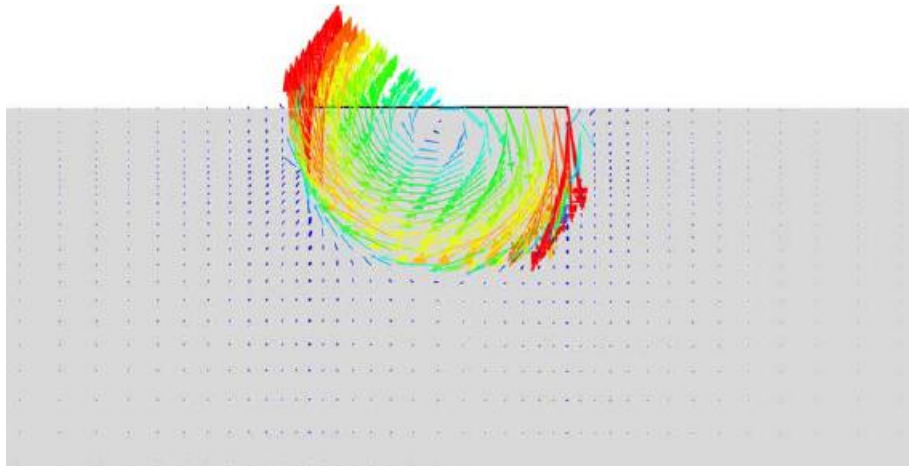
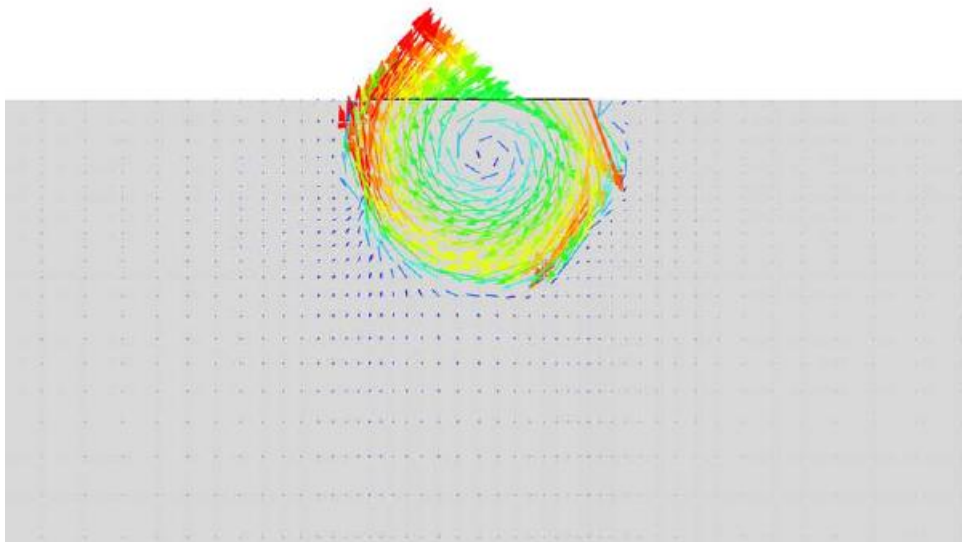


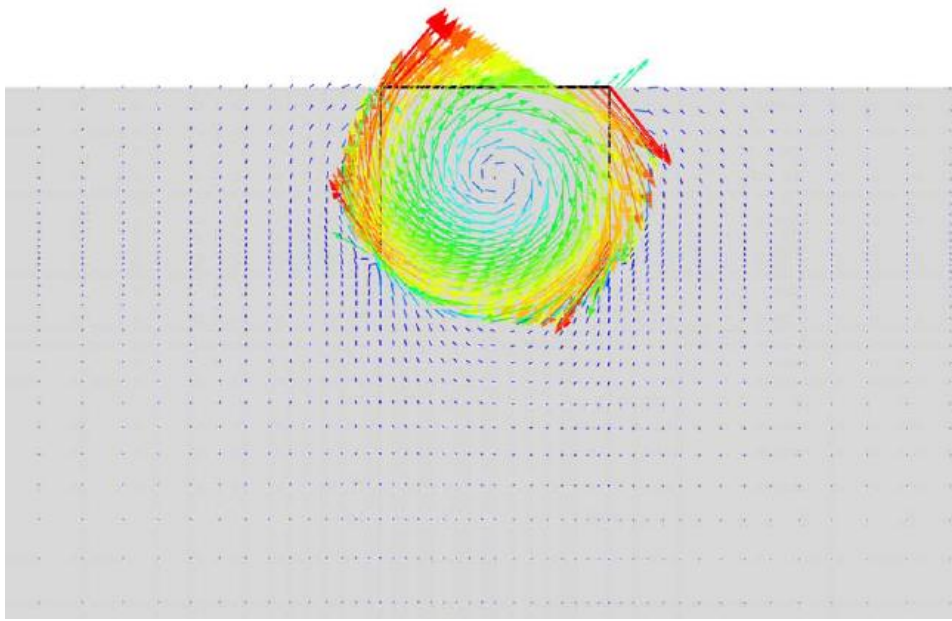
Figure 15: Ultimate moment capacity as a function of embedment ratio



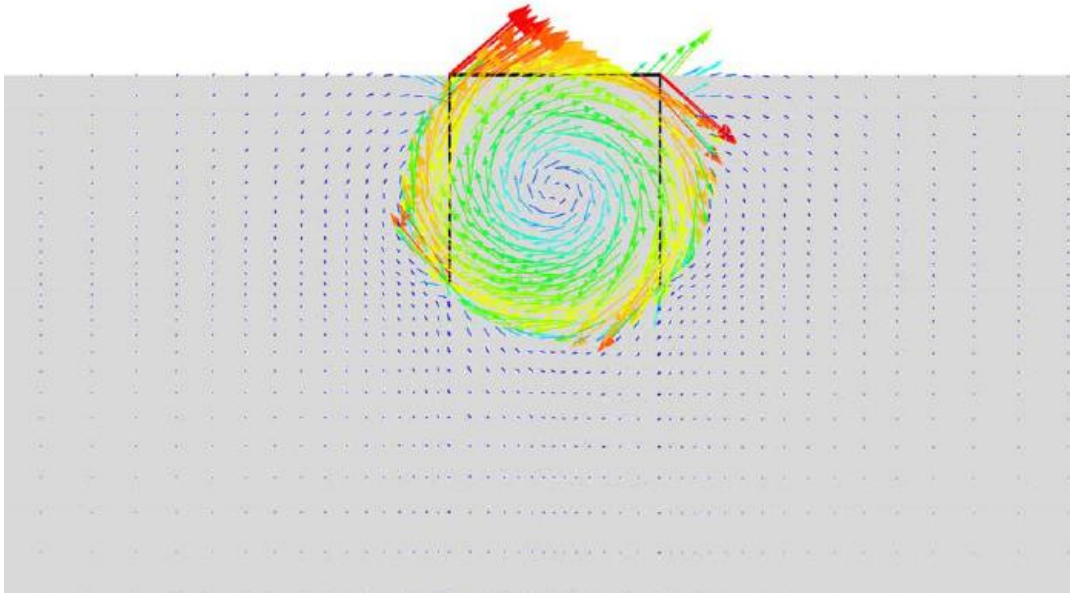
(a)



(b)



(c)



(d)

Figure 16 (a-d): Failure mechanism under moment load (M_{ult} ; u is not constrained), (a) $L/D=0.25$, (b) $L/D=0.5$, (c) $L/D=0.75$, (d) $L/D=1$

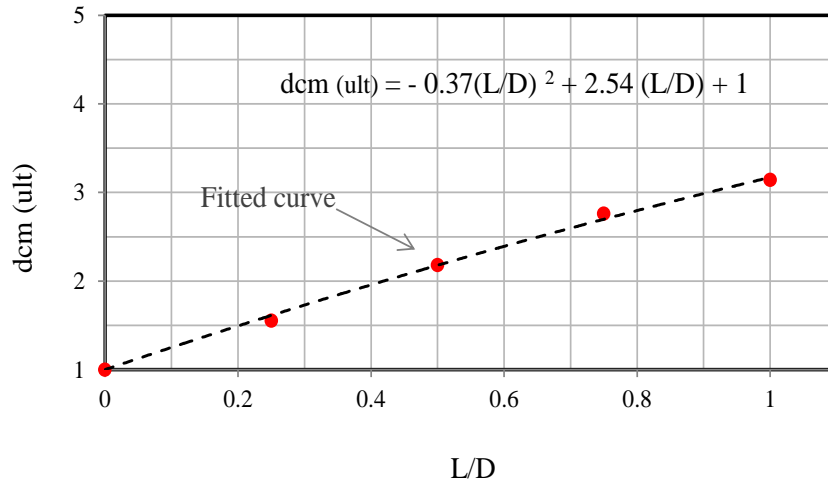


Figure 17: Ultimate moment capacity depth factor as a function of L/D ratios

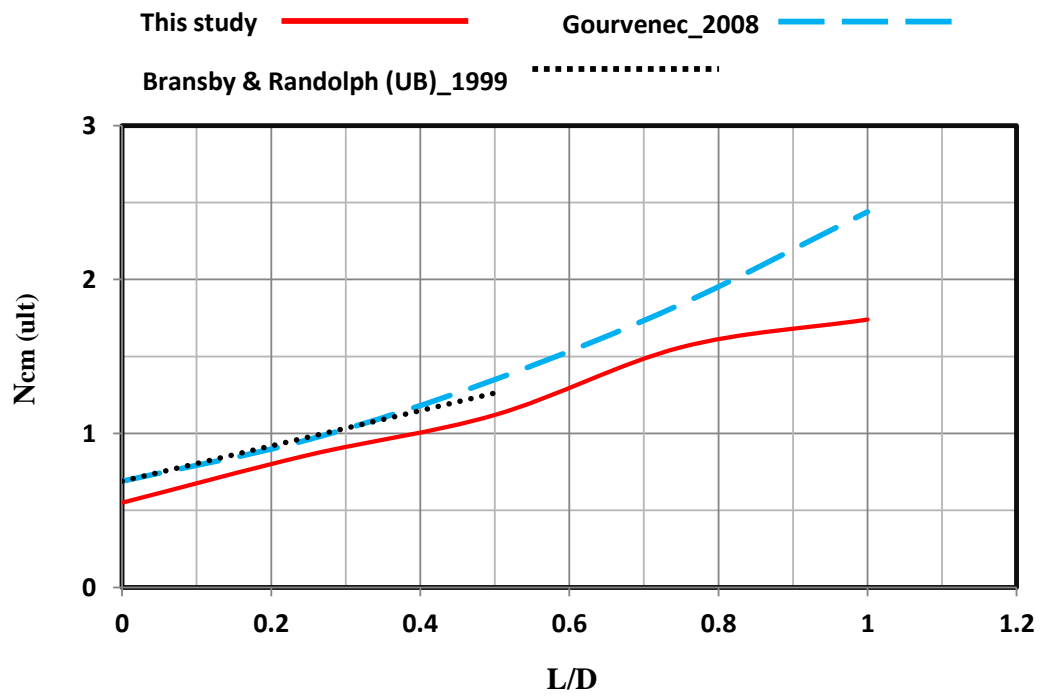


Figure 18: Comparison of ultimate moment bearing capacity factor

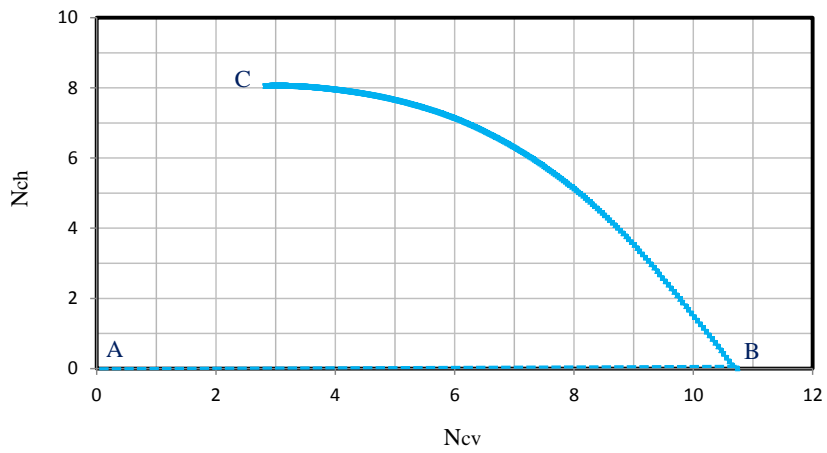


Figure 19: A cross section of yield locus in V-H space using side-swipe method

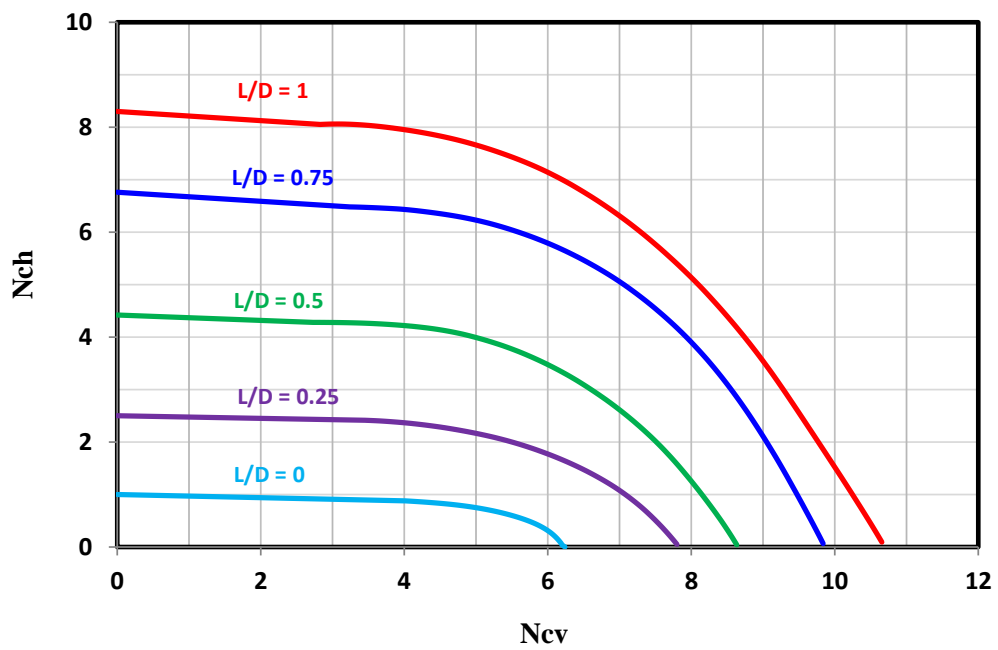


Figure 20: Failure envelopes for vertical and horizontal loading space (moment load = 0)

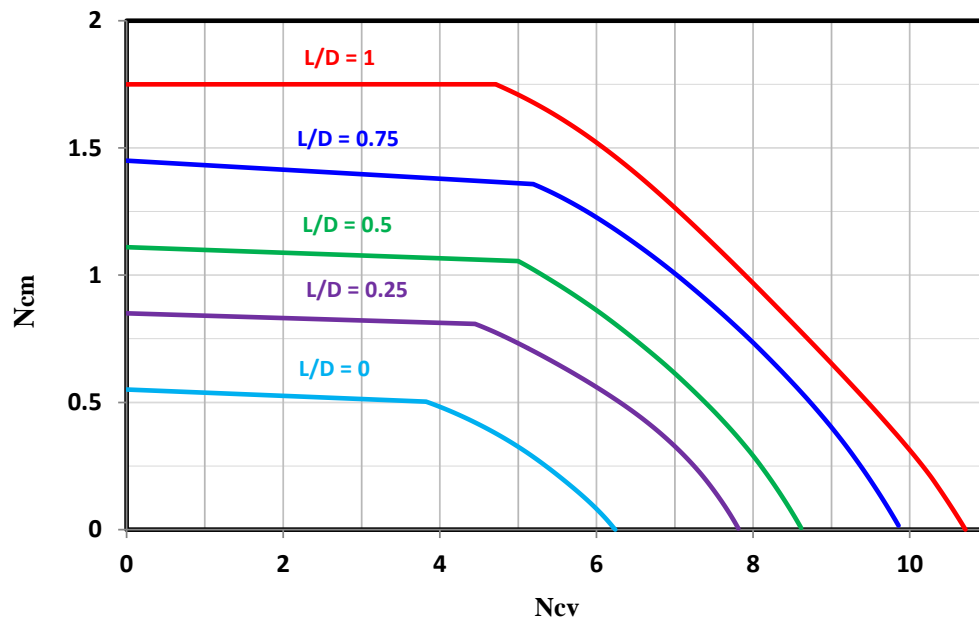


Figure 21: Failure envelopes for vertical and moment loading space (horizontal load = 0)